JMEPEG (2024) 33:4149–4159
https://doi.org/10.1007/s11665-024-09278-w

1059-9495/$19.00

ORIGINAL RESEARCH ARTICLE

Neutron Diffraction Residual Stress Study of a AA2219-T87 Self-Reacting Friction Stir Weld

B.J. Wing, D. Polsky, J.R. Bunn, E.A. Payzant, and C.J. Rawn

Submitted: 8 June 2023 / Revised: 14 October 2023 / Accepted: 7 February 2024 / Published online: 13 March 2024

2219-T87 is a precipitation hardenable aluminum-copper alloy which sees wide use in structural aerospace components. Thick panels of this alloy are joined via self-reacting friction welding (SRFSW); however, this thermomechanical process can result in significant loss of the alloy's strengthening precipitates and large residual stresses which are detrimental to mechanical behavior and performance. High-resolution maps of the residual strain and stress states along the normal, transverse, and longitudinal directions of 2219-T87 SRFSW were obtained using neutron diffraction measurements. Residual stress had the highest tensile value in the heat-affected zone (HAZ) and the largest compressive stress in the base metal region of the normal and transverse directions. Line profile residual stress distributions displayed an "M"-shaped distribution in each direction with the longitudinal direction being the most pronounced while 2D residual stresses displayed an hourglass-shaped pattern. Average maximal longitudinal residual stress values ranged from 60.6 to 85.6% of yield. Microhardness testing across the transverse weld section produced a "V"-shaped curve with slight hardness recovery in the stir zone. Maximal and minimal microhardness values were observed in the base metal (154 HV) and thermomechanically affected zone (82 HV), respectively. Microstructural evolution was recorded using optical microscopy and showed decreasing grain size from the HAZ to the stir zone.

Keywords aerospace, aluminum, metallography, nondestructive testing, residual stress, welding

1. Introduction

Precipitation hardenable 2xxx aluminum alloys possess high strength and ductility, low density, good corrosion resistance, and stable cryogenic performance making them ideal for structural aerospace applications such as liquid propellant rocket fuel tanks (Ref 1). However, joining these alloys via fusion-based processes introduces additional risk for detrimental issues such as porosity, solidification cracking, and loss of mechanical properties (i.e., joint softening) (Ref 1, 2).

Friction stir welding (FSW) is a solid-state process which solves many of the issues associated with fusion-based processes (Ref 1–3). In FSW, a rotating tool consisting of a shoulder and pin travels along abutting or overlapping plates and mixes the joint edges. Frictional heat produced by the rotating tool softens the material while the shearing action of the tool shoulders and pin provides material mixing and bonding of the plates. Careful selection of processing parameters for FSW improves the stability and repeatability weld joint properties when compared to its fusion-based counterparts (Ref 3).

Self-reacting friction stir welding (SRFSW)—sometimes known as bobbin tool friction stir welding or self-support friction stir welding—is a variant of FSW which allows for joining thick and circular plates. SRFSW operates on the same principle as FSW but with an additional shoulder at the end of the pin. The root side shoulder eliminates the need for backing plates, increases efficiency, improves heat distribution and resulting microstructure, and creates high strength welds (Ref 4, 5). However, residual stresses remain a concern.

Residual stresses are stresses present in a solid in the absence of external forces and are the result of misalignments between regions in the material. In the case of SRFSW, these misalignments are primarily the result of differences in thermomechanical deformation within the joint. Accounting for residual stress in weldments is important as they can negatively impact material performance and accelerate failure (Ref 6). Joint softening, a loss of mechanical properties along the weld, in aluminum 2xxx alloys is often due to changes in precipitate size and distribution as well as increased residual stresses. Joint softening has been noted in AA6061, AA6056-T78, and AA2024 SRFSWs though the extent of its effects and relation to residual stresses are not well documented (Ref 5, 7–11). Unfortunately, while residual stress distribution in traditional FSW is widely researched, there is limited research on residual stress for SRFSW and considerably less for this specific alloy.

This invited article is part of a special topical issue of the *Journal of Materials Engineering and Performance* on Residual Stress Analysis: Measurement, Effects, and Control. The issue was organized by Rajan Bhambroo, Tenneco, Inc.; Lesley Frame, University of Connecticut; Andrew Payzant, Oak Ridge National Laboratory; and James Pineault, Proto Manufacturing on behalf of the ASM Residual Stress Technical Committee.

B.J. Wing, D. Polsky, and **C.J. Rawn**, The University of Tennessee Knoxville, Knoxville, TN; **J.R. Bunn** and **E.A. Payzant**, Oak Ridge National Laboratory, Oak Ridge, TN 37831-6393. Contact e-mail: crawn@utk.edu.

Neutron diffraction was selected to comprehensively map the residual strain/stress state. Evaluating residual stress via neutron diffraction offers several key benefits for modeling efforts including high resolution, excellent material penetration allowing for three-dimensional mapping of subsurface residual stresses, bulk measurement, and nondestructive measurement (Ref 12).

In this study, neutron diffraction is employed to measure residual strain and stress in a 2219-T87 SRFSW. Strain and stress evolution within the welds is discussed in conjunction with microhardness and microstructural changes.

2. Experiment/Methods

A thick plate, 2219-T87 SRFSW in butt weld configuration was prepared at NASA Marshall Space Flight Center (MSFC) using proprietary processing parameters and tool design.

2.1 Microstructure

To assist in gauge volume selection and ensure that the neutron diffraction measurements were unaffected by variations in grain size, microstructural analysis of the weld was conducted.

2.1.1 Microscopy. Specimens were sectioned from the weld using wire electrical discharge machining (EDM), mounted in epoxy, and successively ground and polished to 0.05 μm colloidal silica. Two samples were prepared; one was immersed 1% aqueous NaOH for 3 min, and the other was immersed in Weck's reagent for 10 s after which both were removed and rinsed with cold deionized water.

The etched specimens were imaged using a Nikon Eclipse MA200 at magnifications up to 500× in each weld region. A macrograph of the weld joint was constructed by stitching images taken of the sample treated with 1% aqueous NaOH using a Keyence VHX-1000 in *Fiji* (*ImageJ*) (Ref 13). Grain sizes were measured with *ImageJ* using the intercept method according to ASTM E112 (Ref 14).

2.2 Microhardness

Microhardness measurements were performed on an epoxy mounted, ground, and polished transverse weld cross-section of 5-mm thickness. Measurements were taken using a LECO AMH 55 at intervals of 0.75 mm to the sample edge in the normal (y direction) and transverse (x direction) directions using a load of 500 gf (4.903325 N) and 15-s dwell time.

2.3 Neutron Diffraction Measurements

Neutron diffraction measurements were carried out at the High Flux Isotope Reactor (HFIR) of Oak Ridge National Laboratory (ORNL) on the High Intensity Diffractometer for Residual Stress Analysis (HIDRA) (Ref 15, 16). The instrument's incident wavelength is defined by a bent Si crystal focusing Popovici–Stoica monochromator and can be adjusted to suit a variety of materials (Ref 17). The Al (311) reflection was selected for this study as it has a relatively high peak intensity (for more rapid data collection), a high multiplicity (and so less impacted by texture), an elastic modulus very close to the bulk modulus, and is not readily affected by intergranular strains (Ref 12, 18). The Si (331) monochromator setting was used to provide a wavelength of λ = 1.731 Å and a scattering angle of ~ 90° for the Al (311).

The plate center was selected as the origin and coarsely aligned via an optical telescope. Prior to measurements, "edge scans" were performed to account for geometric deviations of the plate and form a virtual coordinate system related to the sample coordinate system. Measurements in the three orthogonal directions (transverse, normal, and longitudinal—Fig. 1) were performed in increments of 1.066 mm along the plate thickness to: ± 70 mm in the longitudinal direction, ± 100 mm in the transverse direction, and from − 100 to 80 mm in the normal direction as measured from the weld centerline.

2.3.1 Gauge Volume. A cubic gauge volume (2 x 2 x 2 mm) was chosen for the longitudinal direction measurement. In the transverse and normal directions, in which weld symmetry can be assumed, a tall, matchstick-like gauge volume (2 x 20 x 2 mm) was chosen to reduce counting and instrument time.

2.3.2 d_0 determination/selection. The thermomechanical nature of the SRFSW process leads to a considerable change in both chemistry and microstructure across the 2219-T87 weld which if unaccounted result in a large difference between apparent and actual strain/stress (Ref 12, 19). Therefore, the determination of a stress-free reference d-spacing, d_0, is essential to obtaining an accurate result.

A stress-free reference (d_0) comb was created after the orthogonal measurements to avoid potential stress relaxation along those directions (Ref 2). This stress-free reference comb allows for mechanical relaxation of local macrostresses and accounts for changes in chemical composition, attributed to the Al-Cu solid solution, and microstructure across the weld. The weld plate was sectioned 234 mm from the weld terminus using a bandsaw to allow for construction of a stress-free reference comb. In constructing the comb, a portion of the weld was sectioned with EDM using 20-mm longitudinal cuts in 4 mm increments from ± 60 mm from the weld centerline. Measurements in the transverse direction were taken at 2.133-mm intervals from the mid-thickness at intervals of 4 mm from the weld centerline 135 mm from the orthogonal measurements. The instrument was aligned to a mark on the weld centerline made during the previous measurement to maintain position consistency.

The d_0 data were obtained using a Si (422) monochromator (λ = 1.540 Å) which provides a scattering angle of ~ 78° for the Al (311). Two rectangular gauge volumes, 2 × 20 × 2 mm and 2 × 10 × 2 mm, were selected for measurement of the transverse direction with the smaller gauge volume centered 15 mm from the plate end to evaluate the effect of the plate sectioning method, Fig. 2. The d-spacing was determined from the measured scattering angle the using a pseudo-Voigt fitting function in PyRS (Ref 20).

2.3.3 Determination of d-spacing, strain, and residual stress. The principle of diffraction/scattering is defined by Bragg's law, Equation 1, which relates the wavelength (λ), interplanar or d-spacing (d), and scattering angle (2θ).

$$\lambda = 2d \sin\theta \quad \text{(Eq 1)}$$

The wavelength is known, and the scattering angle of the measured peak is obtained via peak fitting of the data, rearranging Equation 1, the lattice d-spacing can be calculated from:

$$d = \frac{\lambda}{2 \sin\theta} \quad \text{(Eq 2)}$$

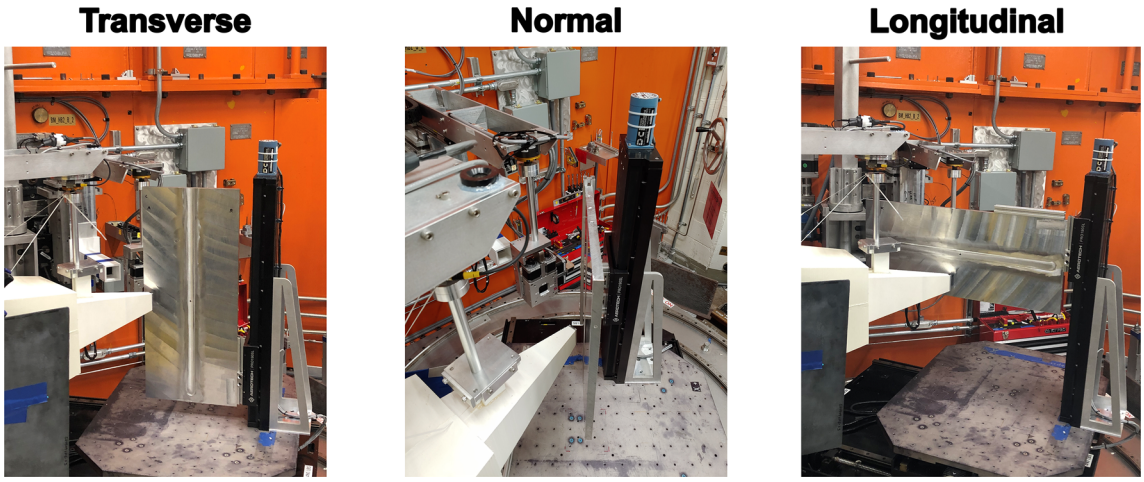

Fig. 1 Images of the weld plate on the beamline at HIDRA HB2B in each measurement orientation

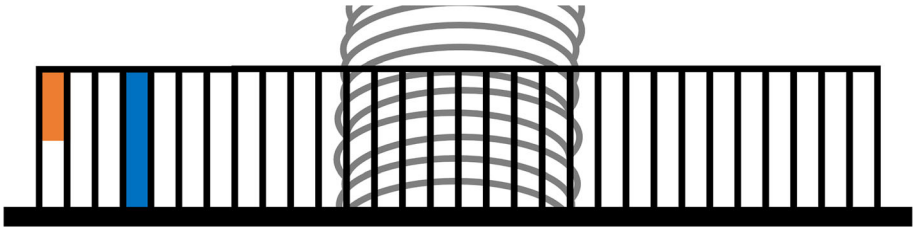

Fig. 2 Stress-free reference comb illustrating large (blue) and small (orange) gauge volumes (Color figure online)

With the d-spacing determined, the residual strain for each principal direction becomes possible by relating the d-spacing difference between the measured point (d) and its stress-free reference (d_0) divided by the stress-free reference d-spacing (d_0).

$$\varepsilon = \frac{d - d_0}{d_0} \quad \text{(Eq 3)}$$

Using the computed residual strain in each principal direction as in Equation 3, the calculation of residual stress becomes possible (Ref 6, 12). Hooke's Law, Equation 4, is applied along with isotropic conditions to provide the following relation, Equation 5:

$$\sigma = E\varepsilon \quad \text{(Eq 4)}$$

$$\sigma_i = \frac{E}{1+v}\left[\varepsilon_{ii} + \left(\frac{v}{1-2v}\right)(\varepsilon_{11} + \varepsilon_{22} + \varepsilon_{33})\right] \quad \text{(Eq 5)}$$

where σ_i is the component of residual stress, E is the elastic (Young's) modulus, v is Poisson's ratio, and ε_{ii} is the component of residual strain.

2.3.4 Model Selection. Residual stress calculations were completed under the assumptions of the Voigt model—in which all grains experience orientation independent uniform strain, and elastic modulus and Poisson's ratio (calculated by averaging the elastic stiffness over all elements of the aggregate) are constant and isotropic (for AA2219-TA7, the average tensile and compressive values are E = 73.1 Gpa and v = 0.33) (Ref 12, 21). The Voigt model is selected as the contributions of *hkl* other than the Al (311) cannot be determined, and error attributable to use of averaged elastic properties is minimal in a static experiment.

2.4 Force Balance

The definition of residual stress as a self-equilibrating stress present in a material in the absence of an external force provides a basis for an alternant d_0 determination and/or correction. Therefore, the sum of all stresses (and moments) must equilibrate across the cross-section provided that the plate is static (i.e., absence of movement or active deformation), which is expressed in Equation 6. The components of stress are defined by the force (F_{ij}) over the area (A) perpendicular to that force, Equation 7. This area is related to the area between measurements and thus the area between the residual stress curve and zero stress value.

$$\Sigma\sigma_{11} = 0;\ \Sigma\sigma_{22} = 0;\ \Sigma\sigma_{33} = 0 \quad \text{(Eq 6)}$$

$$\sigma_{ij} = F_{ij}/A \quad \text{(Eq 7)}$$

2.4.1 Extrapolation. The force and moment balance approach are only valid over the length of the measured cross-section which is the plate width and thickness for this experiment. As the orthogonal direction measurements do not extend the span of this area, extrapolation of existing data points is required. The d-spacing values for d_0 and each orthogonal direction were extrapolated to the plate edges. D-spacing plots for each of these directions are presented in Fig. 3. The average d-spacing difference (Δd) factoring in d_0 assists in the determination of an appropriate extrapolation method, Fig. 4.

The average Δd compared to d_0 is relatively consistent for the transverse and normal directions but continues to increase in the longitudinal direction. This indicates that extrapolation is

reliable in the transverse and normal directions but not in the longitudinal direction. However, further trend evaluation shows that the variation of Δd within each measurement line (thickness) is considerable from point to point and does not follow a discernable trend in any direction, Fig. 5. Error bars are omitted, and Bezier lines used to improve trend observation as such, these lines are not indicative of actual or predicted values between these points.

For this reason, the method evaluated was a constant extrapolation in which the last data points for each direction are held constant and extended throughout the desired range without any algorithmic adjustments.

The force balance approach leads to shifts in d_0 d-spacing values across the plate. This shift can be weighted to reflect individual changes in d-spacing at different locations; however, as the point-to-point correction factor is unknown and significant additional experimentation would be required, only a constant shift—henceforth referred to as a global shift—is considered. The value of this global shift was determined by solving the relation in Equation 6 using the "Goal seek" function in Microsoft Excel and applied.

3. Results

3.1 Macro- and Microstructure

The macrostructure and microstructure of the 2219-T87 SRFSW is presented by Fig. 6 and 7, respectively. The HAZ was noted by coarsened grains compared to the base metal, the TMAZ by elongated and deformed grains, and the stir zone by fine equiaxed grains. Grain size slightly increased from the base metal to the HAZ and decreased significantly to the SZ where it reached a minimum, Fig. 8.

3.2 Microhardness

Mid-thickness microhardness values (± 2-mm thickness) were averaged to create a mid-thickness averaged line graph, Fig. 9 error bars are 1σ. Microhardness values follow a "W-shaped" curve as are characteristic of FSWs. Microhardness values steadily decrease from the BM to the TMAZ and recover in the SZ (~ 97 HV). Highest values are observed in the BM (154 HV) and lowest in the retreating side TMAZ (82 HV).

3.3 Neutron Diffraction

3.3.1 *d*-spacing. D-spacing data for the normal, transverse, and longitudinal directions and d_0 were produced by peak fitting in PyRS. Outlying data points defined by deviations $\geq 1.5\sigma$ were removed and replaced with adjacent values. D_0 values lacked significant outliers and were unchanged. The normal, transverse, longitudinal, and d_0 d-spacing are compared in Fig. 10. In general, the advancing side displays a more rapid change in d-spacing for each direction compared to the retreating side. The highest d-spacing was observed on the advancing side of the longitudinal direction with a slight decrease seen on the retreating side. The lowest d-spacings are seen in the SZ of the normal and transverse directions. Contour plots of the normal, transverse, longitudinal, and d_0 d-spacing are presented in Fig. 11.

3.3.2 FWHM. Weld microstrain and microstructure variation can be expressed in general terms by plotting the full width at half-maximum (FWHM) peak values for the Al (311) as shown in Fig. 12. A clear decrease in the FWHM is observed from the BM to the SZ for all directions.

3.3.3 Strain. Normal, transverse, and longitudinal residual strains were measured and found to follow the characteristic distribution for friction stir welds. The longitudinal residual strain and stress along the weld is "M-shaped" with the advancing side possessing a somewhat higher value compared to the retreating side and an overall decrease in tensile residual strain/stress in and just outside the SZ. The transverse/normal

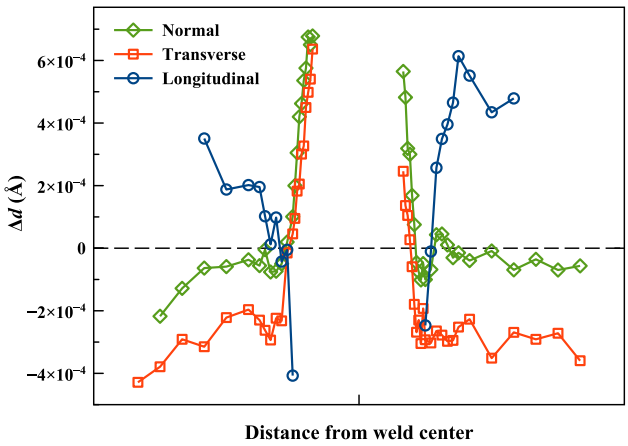

Fig. 4 Average Δd in each direction

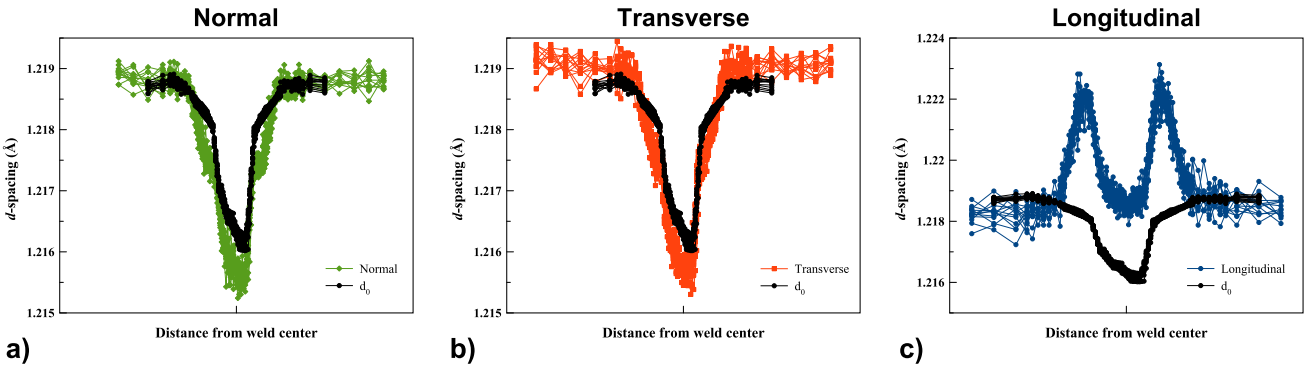

Fig. 3 d-spacing and d_0 comparison in the (a) normal, (b) transverse, and (c) longitudinal direction

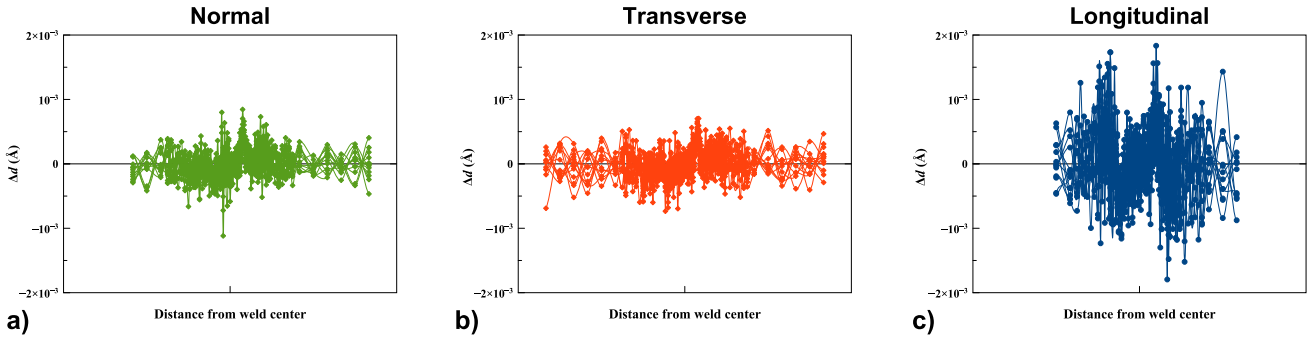

Fig. 5 Δd in the (a) normal, (b) transverse, and (c) longitudinal direction

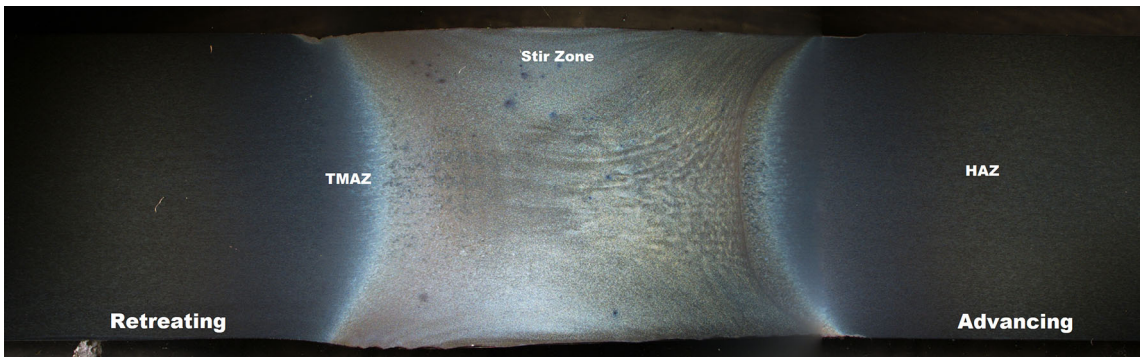

Fig. 6 2219-T87 SRFSW macrograph prepared using 1% aqueous NaOH solution

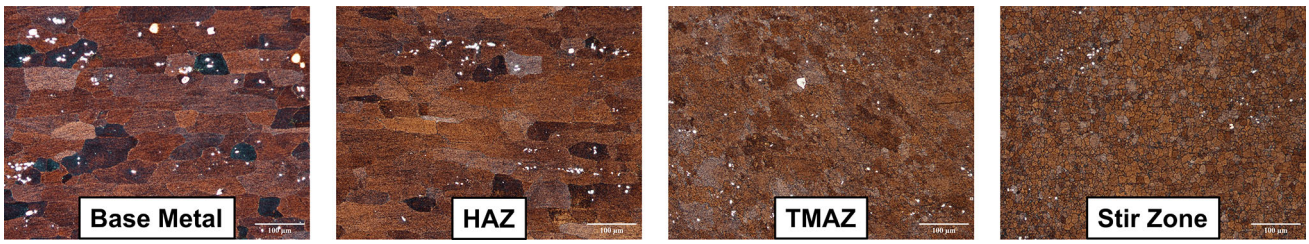

Fig. 7 Micrographs of each weld zone in 2219-T87 SRFSW prepared using Weck's reagent

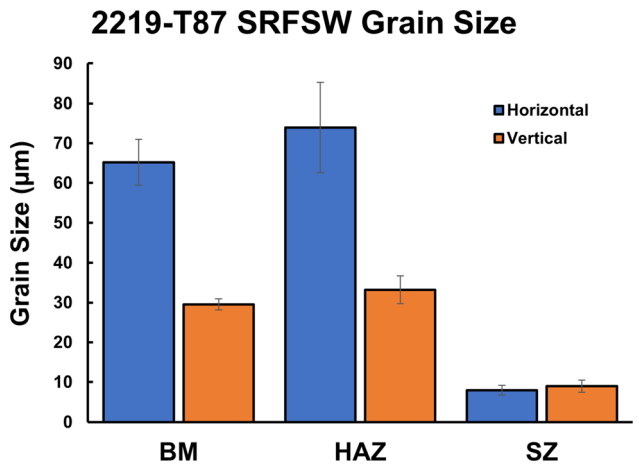

Fig. 8 Horizontal and vertical grain sizes for the BM, HAZ, and SZ with standard deviation

residual strains are slightly "U-shaped" with maxima in the BM and lower in comparison but having the greatest compressive strain/stress values in the SZ (Fig. 13 and 14) (Ref 6).

The maximal longitudinal residual strain occurred on the advancing side just outside the SZ while the minima were in the BM. The normal direction has a maximum tensile strain in the BM and a minimum compressive strain in the SZ. The transverse direction has a comparable minimum compressive microstrain just outside the SZ and a maximal tensile microstrain in the HAZ.

3.3.4 Stress. Residual stress was calculated from Equation 4 using the literature values (E = 73.1 Gpa and ν = 0.33) and residual strain measurements. Figure 15 shows the 1D residual stress plots for each principal direction while Fig. 16 displays the contour plots. The 1D profile shows an "M"-shaped distribution and 2D distribution an hourglass appear-

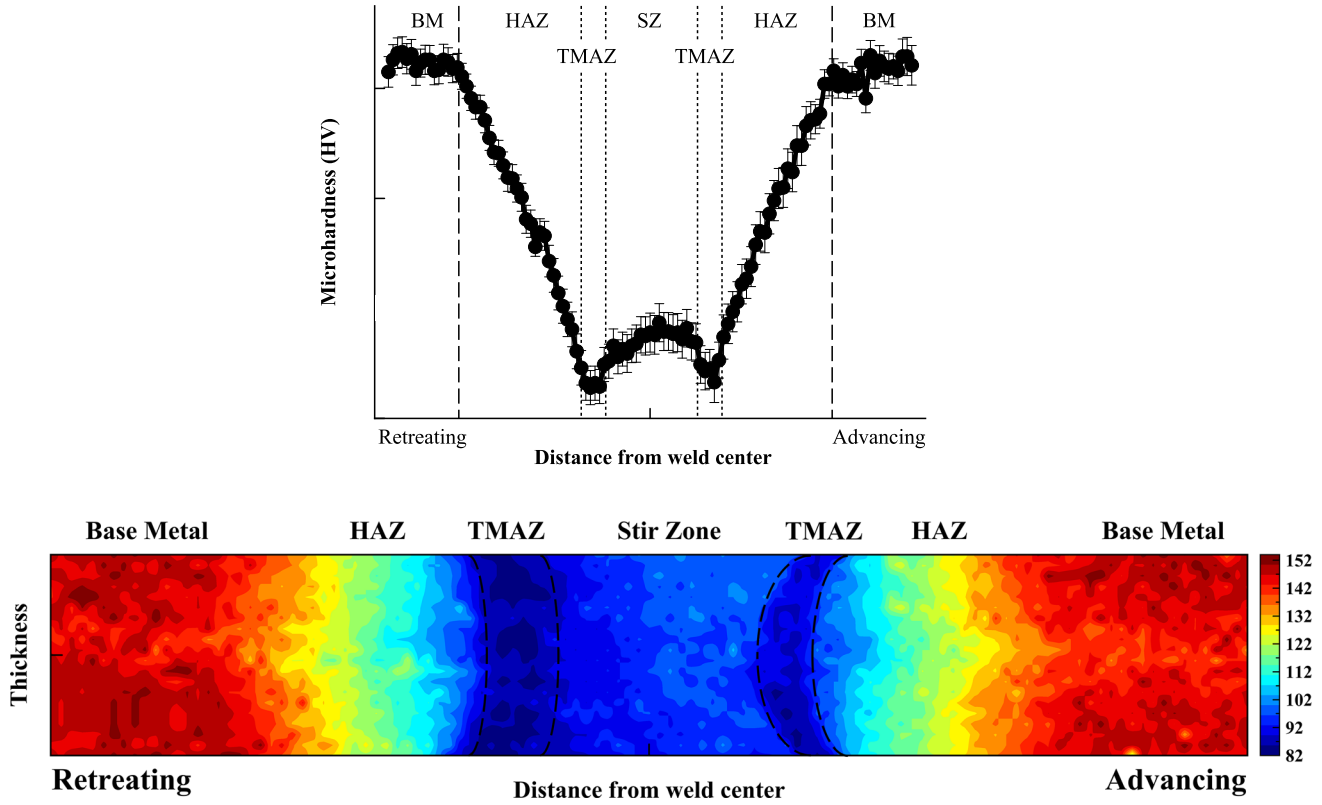

Fig. 9 Microhardness (top) mid-thickness averaged line graph (1σ) (bottom) contour plot with units in HV

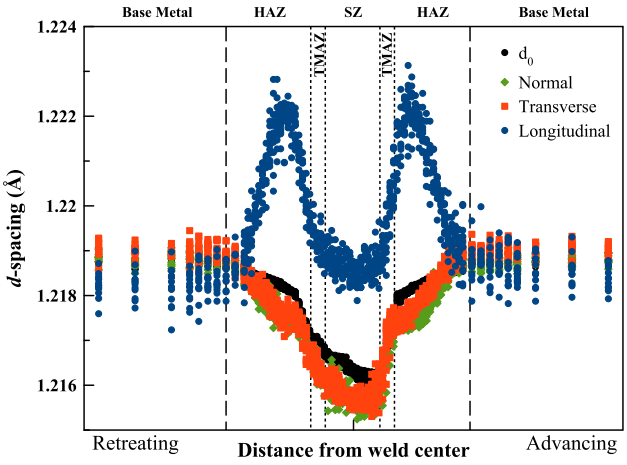

Fig. 10 Normal, transverse, longitudinal, and d_0 d-spacing

ance with the longitudinal component being approximately 3 times greater than the tensile and normal directions. The longitudinal residual stress component maximizes on the advancing side HAZ just before reaching the TMAZ, and the highest compressive value is in the BM. The normal direction's highest tensile residual stress occurred on the advancing side HAZ, and the highest compressive residual stress was in the BM. The transverse direction had similar stress magnitudes with the highest tensile stress in the SZ and highest compressive in the BM. The maximal residual stress is 96.7%, the reported yield stress of 2219-T87, though the average value at this position ranges from 60.6 to 85.6% of yield.

4. Discussion

Residual strain in a 2219-T87 SRFSW was successfully measured via neutron diffraction and used to calculate and map principal residual stresses. Chemical composition and microstructural variation across the SRFSW were accounted for by mechanical relaxation and measurement of a representative weld section.

4.1 Macro–Microstructure

Typical SRFSW macrostructure is observed including the hallmark hourglass-shaped SZ and a sharper TMAZ/SZ transition on the advancing side compared to the retreating side (Fig. 6). The transition differences are consistent with increased advancing side deformation rate and orthogonal grain structure of the BM (Ref 4, 5, 22, 23). There was no indication of weld defects such as voids, joint line remnants, etc.

Four distinct microstructural zones were observed: BM, HAZ, TMAZ, and SZ (Fig. 7). Horizontal and vertical grain size increased from the BM to the HAZ and minimized in the SZ. Grain size measurements in each weld zone were reasonably consistent compared with Anderson-Wedge et al., Table 1 (Ref 24). Observed variation is likely due to a difference in sampled locations within each region and/or processing parameters. Grain size variation between the advancing/retreating sides and upper/lower shoulder was not explored in this study but is expected to be minimal.

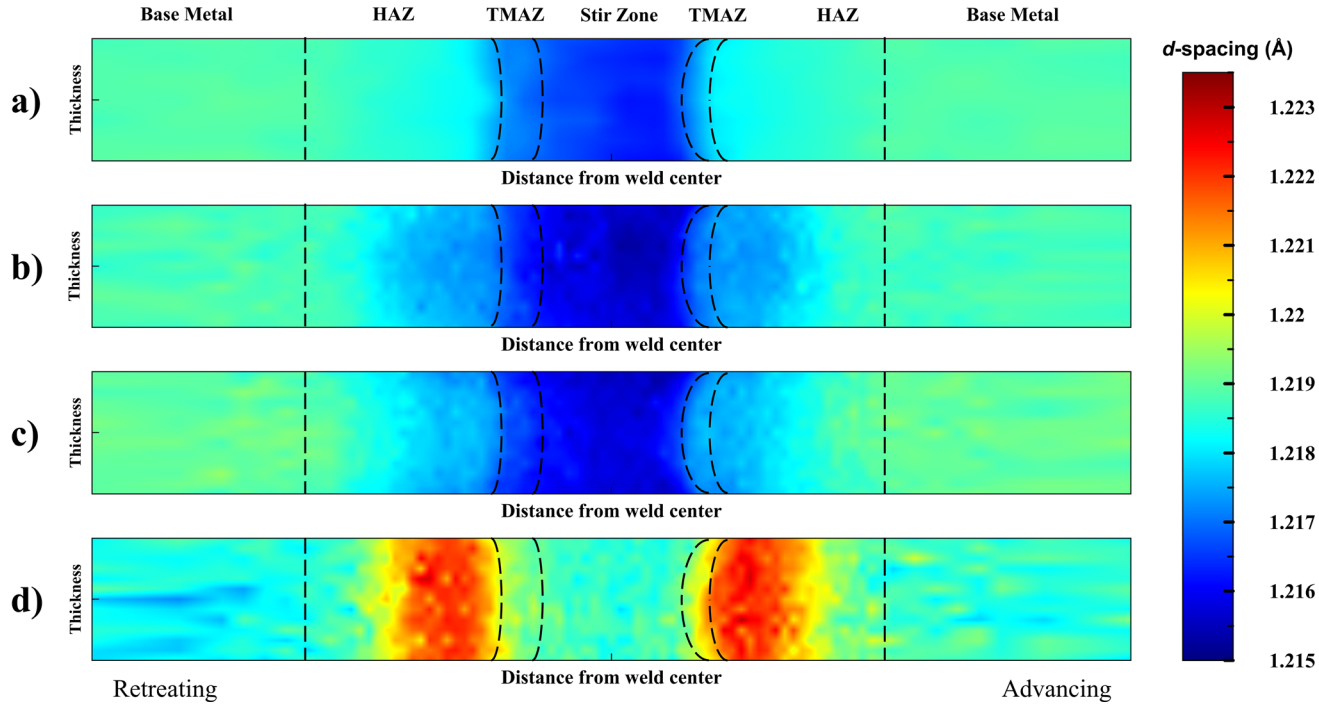

Fig. 11 *d*-spacing contour plots for (a) d_0, (b) normal, (c) transverse, and (d) longitudinal directions

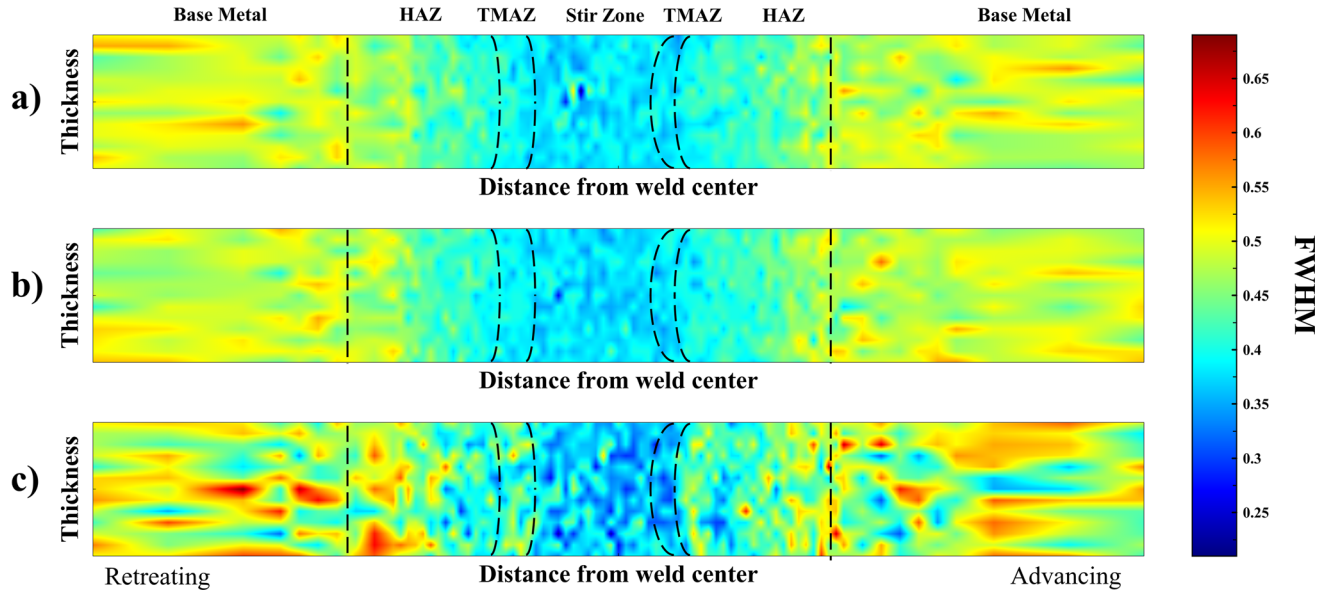

Fig. 12 FWHM contour plots in the (a) normal, (b) transverse, and (c) longitudinal directions

Large grain size ($> 50\ \mu$m) and grain asymmetry can lead to inaccuracy in peak positions and thereby residual strain and stress in neutron diffraction measurements (Ref 25). This grain size-related error was ruled out by ensuring intensity (counts/s) at several locations which was well above background (> 400 counts/s) with well-defined Al (311) peaks for all gauge volumes. Further, normalized peak intensity (I/I_0) change was minimal indicating a lack of "edge effects" associated with abrupt texture change. Peak broadening, as represented by the FWHM, is the result of various contributions such as particle size, dislocations, microstrain, and steep strain gradients (Ref 12). The FWHM shows interesting results that are beyond the scope of this study with decreasing FWHM values from the base metal to the stir zone (Fig. 12). Grain size as a primary contributing factor was ruled out as the FWHM should increase with decreasing crystallite size, and the Scherrer equation is not applicable for the relatively large grain sizes observed. Deconvolution is required to distinguish potential contributions such as dislocations and subgrain size and may warrant further exploration.

4.2 Microhardness

In conjunction with microstructural studies, microhardness profiles can assist in the explanation of physical properties

within a weld. The microhardness profile displays the expected "W"-shaped and "hourglass" appearance for the line graph and contour plot, respectively.

Weld features such as the advancing and retreating sides are readily observed in both the mid-thickness averaged line graph and contour plot. The advancing side is noted by sharper transitions for the HAZ/TMAZ and TMAZ/SZ. The lowest microhardness values are observed on the retreating side of the weld. This aligns with higher expected temperatures on the retreating side compared to the advancing side, resulting in greater precipitate dissolution (Ref 4, 5, 24, 26). The potential strengthening factors for the slight microhardness recovery in the SZ are solid solution strengthening, re-precipitation of fine θ' and θ" particles, and the smaller, equiaxed grains of this region (Ref 2, 27). However, determination of these potential contributions was beyond the scope of this study and therefore not pursued.

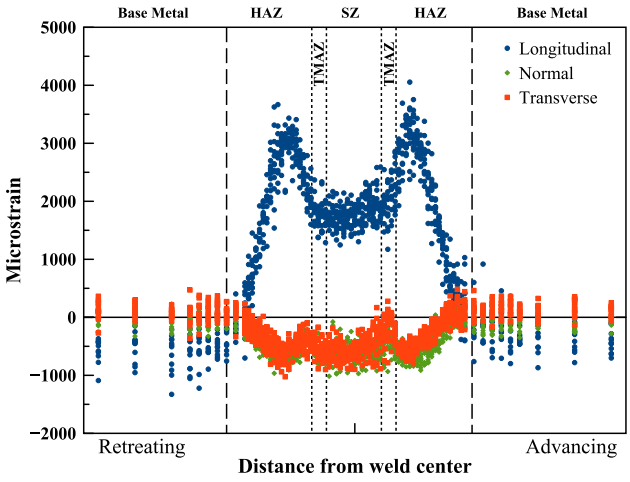

Fig. 13 Residual strain in the normal, transverse, and longitudinal directions

4.3 Strain

The residual strain was determined and found to have the greatest tensile value in the longitudinal direction and most compressive in the normal and transverse directions in the HAZ-SZ-HAZ region. Strain distribution and magnitude align well with expectations exhibiting a slight "W-shape" with local strain peaks at the TMAZ to stir zone transition with the advancing side peak being larger. Local minima of both longitudinal strain and microhardness also occur in this region.

These positions may indicate increased material flow and local shear in this region leading to increased tensile strain/stress as grains are plastically deformed. The possibility of an erroneous strain due to edge effects or texture was evaluated using normalized peak intensity (I/I_0) analysis. This showed no significant intensity variation, indicating that the change is unlikely due to these factors. Another possibility is an offset in d_0 d-spacing measurements leading to a local and erroneous strain/stress in this region; however, insignificant difference was observed upon testing.

4.4 Stress

The residual stress contours appear reasonable and follow expected patterns. The highest compressive stresses lie within the SZ of the normal and transverse directions while the maximum tensile residual stresses occur in the longitudinal direction on the advancing side HAZ. This tensile stress reaches a maximum just below the yield stress for 2219-T87. While limited residual stress data exist for SRFSW, the FSW process typically reports a wide range of residual stress values (20-70% of the yield stress) depending on the welding parameters (Ref 6).

The high value may appear somewhat concerning; however, it is not uncommon for solitary points or sections within a weld to approach the yield stress (Ref 2). Within this context, this residual stress study is atypical in the sense that it represents a

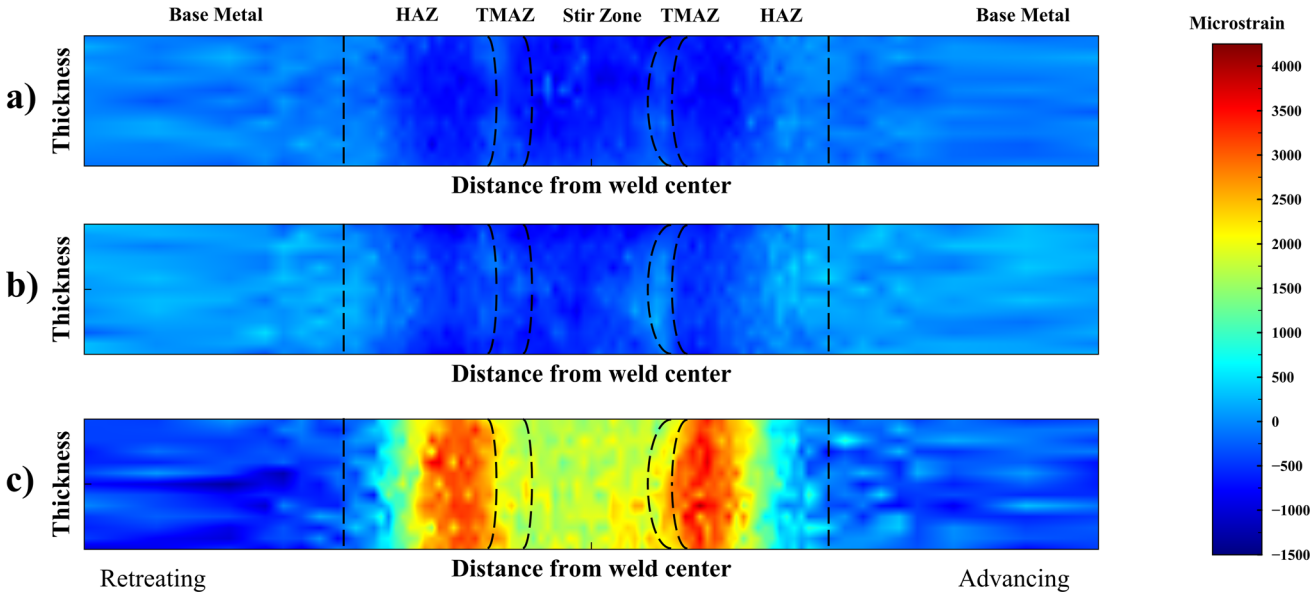

Fig. 14 Residual strain contour plots in the (a) normal, (b) transverse, and (c) longitudinal directions

high-resolution dense mapping scheme thereby presenting enhanced opportunity to detect such values. Further, the average stresses at this location are lower and well in line with the expected maximal residual stress to yield stress ratio and more representative of overall trends.

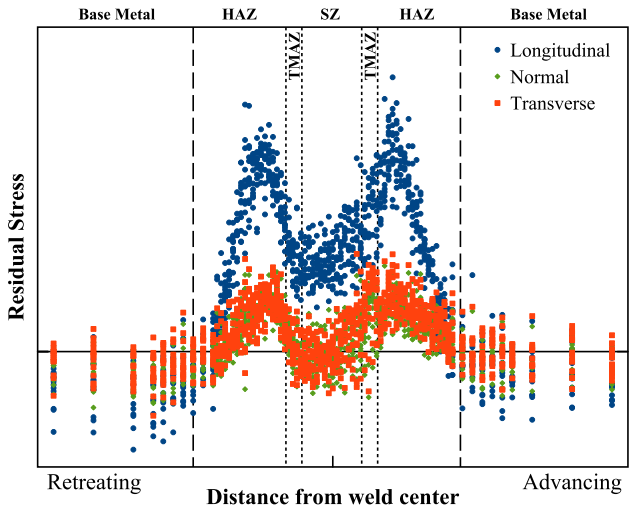

Fig. 15 Residual stress in the normal, transverse, and longitudinal directions

4.4.1 Comparison of the residual stress distribution to prior studies. Residual stress studies of SRFSWs in the literature are limited though do exist for FSW and fusion processes.

In work on similar variable polarity plasma arc (VPPA) welds of 2219-T87 and 2195-T8, Martukanitz et al. employed neutron diffraction on 5-mm weld plates (single pass with 2319 filler) to calculate the residual strain and stress in the longitudinal, normal, and transverse directions (Ref 28). The study observed that peak tensile and compressive residual stresses were related to the position of minimum hardness in the HAZ just outside the fusion zone. The normal and transverse directions were tensile until $\sim$ 16 mm from the fusion zone where they decreased into the compressive region. Maximal tensile residual stresses for the 2219-T87 plate were 50, 10, and 90 MPa for the transverse, normal, and longitudinal directions, respectively. The largest compressive residual stresses were $\sim$ 50 MPa for all directions.

In work on a similar 2219-T87 SRFSW plate of 15.875-mm thickness and proprietary tool and processing parameters, Anderson-Wedge et al. employed x-ray diffraction to determine the surface residual stress (Ref 24). Measurements were taken on the weld crown along the transverse direction to $\pm$ 50 mm from the weld center and $\pm$ 152 mm from the origin along the longitudinal direction. Longitudinal residual stresses values were higher on the advancing side and remained consistent along the weld traverse while those on the retreating side were lower and increased significantly (5.9-109.3 MPa) along the

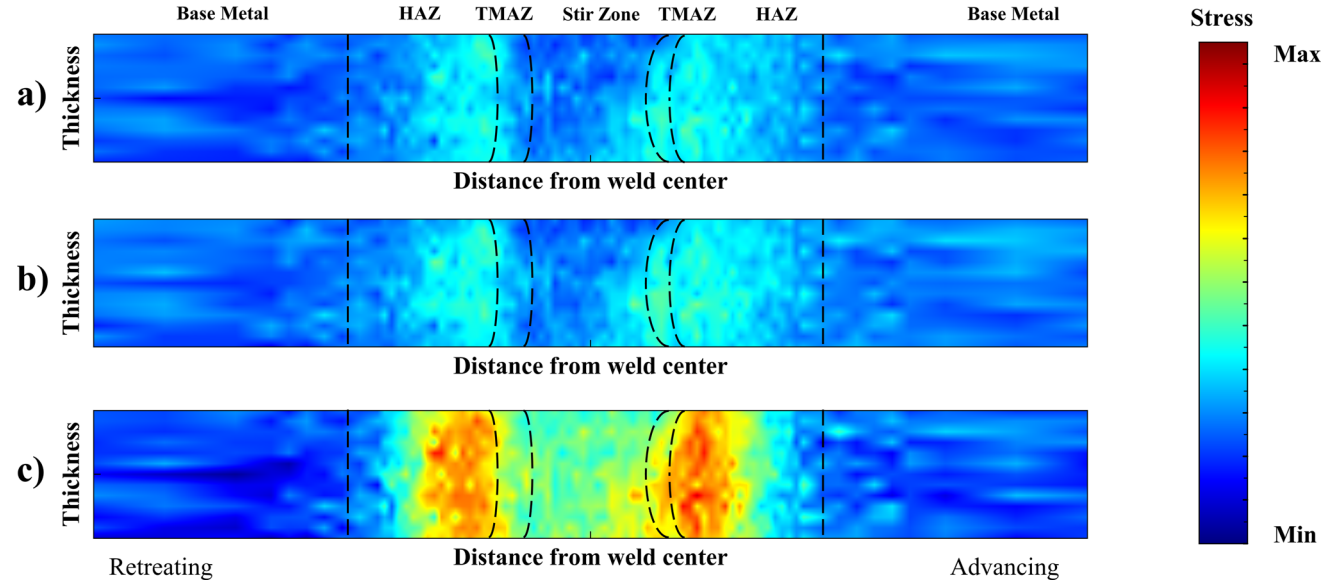

Fig. 16 Residual stress contour plots in the (a) normal, (b) transverse, and (c) longitudinal directions

Table 1 Grain size comparison for 2219-T87 SRFSW

	Horizontal		Vertical	
	Measured	**Anderson-Wedge et al.**	**Measured**	**Anderson-Wedge et al.**
Base metal	65.2 $\pm$ 5.8	49 $\pm$ 14.1	29.5 $\pm$ 1.4	26 $\pm$ 2.3
HAZ	73.9 $\pm$ 11.30	66 $\pm$ 6.9	33.2 $\pm$ 3.5	28 $\pm$ 1.6
Stir zone	8 $\pm$ 1.2	8-12 $\pm$ 0.3-0.5	9 $\pm$ 1.5	8-12 $\pm$ 0.3-0.5
All units in μm.				

weld. The maximal longitudinal residual stress was 117 MPa and occurred in the stir zone. The minimal longitudinal residual stress achieved was − 94 MPa at the retreating side TMAZ. Transverse residual stresses were generally compressive with a minimum of − 75.3 MPa.

We have observed higher magnitudes of residual stress compared to the above studies but with a similar residual stress distribution in the longitudinal direction. However, the normal and transverse directions differed from expectations in that both displayed an "M"-shaped curve instead of a more compressive "U"- or "V"-shaped profile. The 1D residual stress distributions are similar to prior FSW studies; however, the 2D residual stress distributions possess an hourglass appearance unlike FSW though typical of SRFSW macrostructure. The differences can be attributed to the differences to the welding technique (VPPA and FSW vs SRFSW), increased sampling, and the use of neutron diffraction to determine residual stresses in internal locations compared to surface residual stresses via x-ray diffraction.

5. Conclusion

Neutron diffraction was conducted to determine residual strain and stress maps across a 2219-T87 SRFSW. Microstructure and grain size were comparable to prior studies. Microhardness varied in close correlation with residual stress in the HAZ, TMAZ, and SZ. One-dimensional residual stresses displayed an "M"-shaped distribution and 2D residual stresses an hourglass appearance in each direction with the longitudinal direction being approximately 3 times greater than the normal and transverse directions. Maximum longitudinal residual stresses were significant and approached the yield stress of the alloy in the advancing side HAZ near the TMAZ though the average value at this position was within 60.6-85.6% of yield. Minimal residual stresses were observed in the BM for the longitudinal direction and SZ for the normal and transverse directions.

This paper offers understanding of residual stress behavior in 2219-T87 SRFSW via neutron diffraction determination of 1D and 2D normal, transverse, and longitudinal residual stresses.

Acknowledgments

The authors would like to acknowledge partial support though the Manufacturing and Materials Joining Innovation Center (Ma^2JIC), University of Tennessee, Knoxville site. Ma^2JIC is funded by the National Science Foundation (NSF) through the Industry/University Cooperative Research Center (I/UCRC) program award number IIP 1822186. This research used resources at the High Flux Isotope Reactor a DOE Office of Science User Facility operated by the Oak Ridge National Laboratory. The authors would like to thank Kevin Sisco for his contribution and assistance in microhardness testing.

References

1. R. Mishra and H. Sidhar, *Friction Stir Welding of 2XXX Aluminum Alloys Including Al-Li Alloys*, Elsevier, Amsterdam, 2017. https://doi.org/10.1016/C2015-0-04519-1
2. P.L. Threadgill, A.J. Leonard, H.R. Shercliff, and P.J. Withers, Friction Stir Welding of Aluminium Alloys, *Int. Mater. Rev.*, 2009, **54**(2), p 49–93
3. J. Defalco, Friction Stir Welding vs. Fusion Welding, *Weld. J.*, 2006, **85**(3), p 42–44
4. K. Fuse and V. Badheka, Bobbin Tool Friction Stir Welding: A Review, *Sci. Technol. Weld. Join.*, 2019, **24**(4), p 277–304
5. G.-Q. Wang, Y.-H. Zhao, and Y.-Y. Tang, Research Progress of Bobbin Tool Friction Stir Welding of Aluminum Alloys: A Review, *Acta Metall. Sin. (Engl. Lett.)*, 2020, **33**(1), p 13–29
6. W. Woo, Z. Feng, X. Wang, and S.A. David, Neutron Diffraction Measurements of Residual Stresses in Friction Stir Welding: A Review, *Sci. Technol. Weld. Join.*, 2011, **16**(1), p 23–32
7. R.K. Gupta, R. Panda, A.K. Mukhopadhyay, V.A. Kumar, P. Sankaravelayutham, and K.M. George, Study of Aluminum Alloy AA2219 After Heat Treatment, *Metal Sci. Heat Treat.*, 2015, **57**, p 350
8. H.J. Liu, J.C. Hou, and H. Guo, Effect of Welding Speed on Microstructure and Mechanical Properties of Self-Reacting Friction Stir Welded 6061-T6 Aluminum Alloy, *Mater. Des.*, 2013, **50**, p 872–878
9. L. Trueba, M.A. Torres, L.B. Johannes, and D. Rybicki, Process Optimization in the Self-Reacting Friction Stir Welding of Aluminum 6061-T6, *Int. J. Mater. Form.*, 2018, **11**(4), p 559–570
10. A.L. Lafly, D. Alléhaux, F. Marie, C. Dalle Donne, and G. Biallas, Microstructure and Mechanical Properties of the Aluminium Alloy 6056 Welded by Friction Stir Welding Techniques, *Weld. World*, 2006, **50**(11–12), p 98–106
11. F. Marie, D. Allehaux, and B. Esmiller, Development of the Bobbin Tool Technique on Various Aluminium Alloys, in Fifth International Symposium on Friction Stir Welding, Metz (2004)
12. M.T. Hutchings Ed., *Introduction to the Characterization of Residual Stress by Neutron Diffraction*, Taylor & Francis, Boca Raton, 2005
13. C.A. Schneider, W.S. Rasband, and K.W. Eliceiri, NIH Image to ImageJ: 25 Years of Image Analysis, *Nat. Methods*, 2012, **9**(7), p 671–675
14. E04 Committee, Test Methods for Determining Average Grain Size, in ASTM International, n.d., https://doi.org/10.1520/E0112-13R21
15. P. Cornwell, J. Bunn, C.M. Fancher, E.A. Payzant, and C.R. Hubbard, Current Capabilities of the Residual Stress Diffractometer at the High Flux Isotope Reactor, *Rev. Sci. Instrum.*, 2018, **89**(9), p 092804
16. J.R. Bunn, C.M. Fancher, E.A. Payzant, P.A. Cornwell, W.B. Bailey, and R. Gregory, The High Intensity Diffractometer for Residual Stress Analysis (HIDRA), a Third Generation Residual Stress Mapping Neutron Diffractometer at the High Flux Isotope Reactor, *Rev. Sci. Instrum.*, 2023, **94**(3), p 035101
17. M. Popovici, A.D. Stoica, C.R. Hubbard, S. Spooner, H.J. Prask, T.H. Gnaeupel-Herold, P.M. Gehring, and R.W. Erwin, Multiwafer Focusing Neutron Monochromators and Applications, *Neutron Optics*. J.L. Wood, I.S. Anderson Ed., SPIE, San Diego, 2001, p 21–32
18. G.A. Webster, Polycrystalline Materials—Determinations of Residual Stresses by Neutron Diffraction, ISO/TTA3 Technology Trends Assessment, Geneva (2001)
19. L. Vegard, Die Konstitution der Mischkristalle und die Raumfüllung der Atome, *Z. Physik*, 1921, **5**(1), p 17–26
20. C.M. Fancher, J.R. Bunn, J. Bilheux, W. Zhou, R.E. Whitfield, J. Borreguero, and P.F. Peterson, *pyRS*: A User-Friendly Package for the Reduction and Analysis of Neutron Diffraction Data Measured at the

High Intensity Diffractometer for Residual Stress Analysis, *J. Appl. Crystallogr.*, 2021, **54**(6), p 1886–1893
21. J.R. Davis Ed., *Metals Handbook Desk Edition*, 2nd ed. ASM International, 1998 https://doi.org/10.31399/asm.hb.mhde2.9781627081993
22. W.Y. Li, T. Fu, L. Hütsch, J. Hilgert, F.F. Wang, J.F. dos Santos, and N. Huber, Effects of Tool Rotational and Welding Speed on Microstructure and Mechanical Properties of Bobbin-Tool Friction-Stir Welded Mg AZ31, *Mater. Des.*, 2014, **64**, p 714–720
23. D. Alléhaux and F. Marie, Mechanical and Corrosion Behaviour of the 2139 Aluminium-Copper Alloy Welded by the Friction Stir Welding Using the Bobbin Tool Technique, *MSF*, 2006, **519–521**, p 1131–1138
24. K. Anderson-Wedge, G. Stubblefield, N. Zhu, B. Long, S.R. Daniewicz, P. Allison, J. Sowards, O. Rodriguez, and R. Amaro, Characterization of the Evolution of 2219-T87 Aluminum as a Function of the Friction Stir Welding Process, *Int. J. Fatigue*, 2021, **142**, p 105954
25. A.D. Krawitz, *Introduction to Diffraction in Materials, Science, and Engineering*, Wiley, New York, 2001
26. Q. Wen, W. Li, V. Patel, Y. Gao, and A. Vairis, Investigation on the Effects of Welding Speed on Bobbin Tool Friction Stir Welding of 2219 Aluminum Alloy, *Met. Mater. Int.*, 2020, **26**(12), p 1830–1840
27. Y.C. Chen, J.C. Feng, and H.J. Liu, Precipitate Evolution in Friction Stir Welding of 2219-T6 Aluminum Alloys, *Mater Charact*, 2009, **60**(6), p 476–481
28. R.P. Martukanitz, P.R. Howell, E.A. Payzant, S. Spooner, and C.R. Hubbard, Neutron Diffraction Studies of Welds of Aerospace Aluminum Alloys, in Oak Ridge National Lab. (ORNL), Oak Ridge (1996)